

Chapter 7

Cos-theta Nb₃Sn Dipole for a Very Large Hadron Collider



Alexander V. Zlobin

Abstract A series of 1 m long Nb₃Sn dipole models with a magnetic field of 10–11 T in a 43.5 mm bore was developed at FNAL as part of a research and development effort for a Very Large Hadron Collider. This chapter describes the magnet design in single-aperture and twin-aperture configurations, details of the magnet short model fabrication, and summarizes the results of magnetic, mechanical, and quench protection analyses, and model test results.

7.1 Introduction

In 1998 the Fermi National Accelerator Laboratory (FNAL, also known as Fermilab), in collaboration with the Lawrence Berkeley National Laboratory (LBNL) and the High Energy Accelerator Research Organization (KEK), Japan, started a new high-field accelerator magnet research and development (R&D) program with the goal of developing a cost-effective and robust magnet design and technology for a post-LHC Very Large Hadron Collider (VLHC). VLHC studies showed that a nominal operating field between 10 and 12 T is optimal to provide adequate radiation beam damping without significant complication of the machine's cryogenic and vacuum systems (Fermilab 2001). The VLHC target operating fields excluded using the traditional Nb-Ti magnet technology due to the low upper critical magnetic field for this superconductor. Alternative superconductors for high-field accelerator magnets are the A15 materials, primarily Nb₃Sn. Ternary Nb₃Sn composite wires with an upper critical magnetic field of ~24 T at 4.2 K and a critical temperature of ~18 K were already being produced by industry on a fairly large scale.

Although the work on Nb₃Sn accelerator magnets started in the 1960s, just a few years after the discovery of this material, it was only in the 1990s that some Nb₃Sn short dipole magnets exceeded the 10 T magnetic field threshold (see Chap. 3). All of those magnets were shell-type (also known as cos-theta) dipoles with a bore diameter

A. V. Zlobin (✉)
Fermi National Accelerator Laboratory (FNAL), Batavia, IL, USA
e-mail: zlobin@fnal.gov

of 50 mm. Two 1 m long dipole models, Model Single of the University of Twente (MSUT), the Netherlands and D20 by LBNL, reached 11.4 T and 12.5 T, respectively, at 4.5 K (den Ouden et al. 1997; McInturff et al. 1997) (see also Chaps. 5 and 6). None of those magnets, however, were of accelerator quality, focusing mostly on reaching high fields.

Progress in raising the critical current density of commercial Nb₃Sn composite wires in the late 1990s made it possible to design cost-effective Nb₃Sn accelerator magnets with a nominal field of 10–12 T. Extensive studies of shell-type and block-type dipole designs with small apertures, various current block arrangements and cable parameters, etc., were carried out at FNAL with the goal of finding optimal magnet parameters and robust, cost-effective designs and technologies for high-field dipoles suitable for a VLHC (Ambrosio et al. 2000a; Sabbi et al. 2000). This chapter summarizes the magnetic and mechanical design studies, describes basic magnet design and fabrication technology, as well as specific features and parameters of the cos-theta Nb₃Sn dipole developed at FNAL for the VLHC in the framework of the High-Field Magnet (HFM) R&D program. Tests results for the first series of Nb₃Sn accelerator magnets are presented and discussed.

7.2 Design Studies

The work started with conceptual design studies of cos-theta dipoles for VLHC. These studies were first performed to select optimal magnet aperture, nominal operating field and operating margins, conductor and iron yoke parameters as well as to estimate field quality, Lorentz forces, stored energy, and magnet inductance (Ambrosio et al. 2000a). These studies used the parameters of superconducting composite wires developed and produced at the time by Intermagnetics General Corporation based on the internal tin (IT) process. The wire critical current density at 12 T and 4.2 K was 1.9 kA/mm², the Cu/non-Cu ratio was 0.85, and the copper matrix residual resistivity ratio (RRR) was 100. Two types of Rutherford cable were used in the analysis. Cable 1 consisted of 28 strands, 1 mm in diameter, had 14.23 mm width, 1.8 mm mid-thickness, and 1° keystone angle. Cable 2 consisted of 38 strands, 0.808 mm in diameter, had 15.4 mm width, 1.46 mm mid-thickness, and 0.5° keystone angle. The thickness of the cable insulation was 0.125 mm, which corresponded to the commercially available S2-glass tape and to the ceramic insulation developed at that time at Composite Technology Development, Inc. (CTD).

Several opposing requirements were considered to select the magnet aperture size. A large magnet aperture helps to achieve good field quality, and simplify the design of the beam screen and the coil ends. A small magnet aperture reduces the magnet stored energy, the inductance, and the mechanical stresses. It also decreases the coil mass size and, thus, the magnet's cost.

To choose the preliminary coil cross-sections, the following constraints were imposed: (a) a range of coil aperture of 30–50 mm; (b) a target design field of 12 T; (c) no coil grading; and (d) low-order geometrical harmonics below 1 unit

Table 7.1 Magnet design comparison

Design option	Cable 1			Cable 2
	I	II	III	IV
Bore diameter (mm)	50	45	40	40
Turns per dipole	64	60	52	64
Max. bore field B_{ss} (T)	12.4	12.4	12.5	12.5
Max. magnet current I_{ss} (kA)	16.8	16.8	18.5	15.4
Stored energy at 11 T (kJ/m)	289	256	221	230
Inductance (mH/m)	2.75	2.32	1.67	2.53
Coil area (cm ²)	32.8	30.7	26.6	28.8
Min. pole width (mm)	17.5	16.2	15.0	14.6

(10^{-4} parts of the main field). A collarless structure with a 9 mm gap between coil and yoke was chosen, and no iron saturation effect was anticipated. To simplify coil fabrication, coil turns were positioned radially, and the minimal width of the coil inner-layer pole was 13 mm. The latter requirement was based on previous coil winding experience and on special cable winding tests.

Magnet cross-sections were analyzed using the ROXIE code (Russenschuck 1995). Pre-selected designs were compared based on transfer function (TF), stored energy, inductance, coil mechanical stress, and some other parameters. Designs I–III used Cable 1 and had a coil aperture of 50, 45, and 40 mm respectively. Design IV used Cable 2 and had a 40 mm aperture. For each case it was possible to achieve field quality to the level of the field quality requirements for the Superconducting Super Collider (SSC) dipoles (Jackson 1986). Coil cross-sections with 30 mm and 35 mm aperture and rather good field quality were also studied, but they were rejected due to potential coil winding problems.

Table 7.1 summarizes the main parameters of the pre-selected dipole designs. For all four magnets the maximum bore field exceeds 12 T. While the number of turns decreases by 20% as the bore diameter reduces from 50 to 40 mm, the magnet current increases only by 9%, the stored energy reduces by 25%, and the inductance decreases by 35%. A significant saving of superconductor was achieved in magnets with the smallest coil aperture. The minimal pole width and the cable block position for each preselected design ensured easy cable windability.

The maximum stress in each of the four coils due to Lorentz forces was less than 100 MPa at 11 T. It is much less than the threshold value of 150 MPa, at which the critical current degradation of Nb₃Sn strands becomes significant and irreversible. Since Lorentz forces and stresses become smaller when the coil diameter decreases, a lower coil azimuthal pre-stress at room temperature is required.

The analysis showed that there were many good reasons to reduce the magnet aperture diameter. On the other hand, the analysis of the persistent current effect revealed some benefits of having larger apertures. The sensitivity of field harmonics to block displacements also decreases as the aperture increases. Iron saturation effects did not add any strong restrictions to the cross-section choice, although a smaller iron yoke diameter would have helped reducing the magnet's weight and cost.

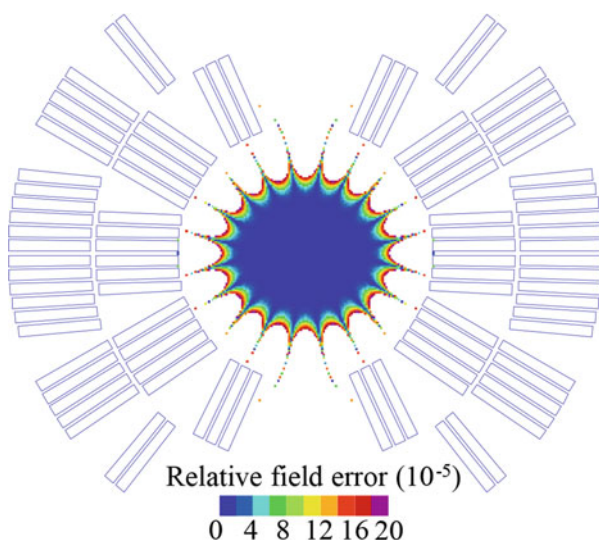
In addition to the pros and cons above, the final choice for the magnet cross-section was made by also taking into account the availability of the magnet fabrication infrastructure and tooling at FNAL, and specifically the availability of equipment from the high gradient quadrupole program for the LHC interaction regions. To make robust coils and reduce the risk of turn-to-turn shorts, the cable insulation thickness was increased to 0.25 mm. With these additional considerations, a coil cross-section with 43.5 mm bore diameter and 400 mm outer diameter yoke was eventually selected.

7.3 Magnet Design and Parameters

The geometrical parameters of the Rutherford cable used to optimize the coil cross-section were similar to Cable 1, described in the previous section. The cable consists of 28 1 mm strands, has a width of 14.24 mm, a thin edge of 1.687 mm, and a thick edge of 1.913 mm. The cable packing factor is 0.884. The cable insulation is 0.25 mm thick.

The optimized coil cross-section of the cos-theta dipole is shown in Fig. 7.1. Each coil consists of 24 turns: 11 in the inner layer and 13 in the outer layer. The thickness of the inter-layer insulation is 0.28 mm, and the thickness of the mid-plane insulation spacers is 0.125 mm per quadrant for both layers. Pole blocks are integrated into the coil inner and outer layers. The optimized width of the inner-layer pole is 15.09 mm, which is convenient for coil winding. Each coil has four wedges per side, two for each layer, which are used to minimize the low-order geometrical harmonics and ensure the radial turn position. To decrease the maximum field and improve the field quality in the magnet ends, the coil end design also has a block-wise arrangement with the same number of blocks and turns per block as in the magnet body.

Fig. 7.1 Coil cross-section



7.3.1 Single-Aperture Design and Parameters

The field distribution diagram and the cross-section of the single-aperture dipole magnet are shown in Fig. 7.2. To reduce magnet cost, the traditional collars are replaced with 8 mm thick coil–yoke spacers. The iron yoke has an inner diameter of 120 mm and an outer diameter of 400 mm. The yoke length of 600 mm is shorter than the coil length, which allows reducing the coil end fields and maximizing the length of uniform field in the magnet aperture. The coils are supported by a vertically split iron yoke, locked with two aluminum clamps, and by the stainless-steel skin.

The coil–yoke spacers protect the coil during magnet assembly. The coils are aligned relative to the spacers via two vertical extensions in the outer-layer pole posts, whereas the spacers are centered inside the yoke via two mid-plane keys. The interference of spacer and pole extension guarantees their contact during magnet assembly and operation.

Calculated magnet design parameters are shown in Table 7.2. A noticeable reduction of coil area was achieved in this design compared with earlier Nb₃Sn magnets with similar design fields. The coil cross-section area is smaller than that in the MSUT (design field of 11.4 T) (den Ouden et al. 1997) by a factor of ~2 and than that in D20 (design field of 13.4 T) (McInturff et al. 1997) by a factor of 3. Notice that all those magnets have a slightly larger bore of 50 mm.

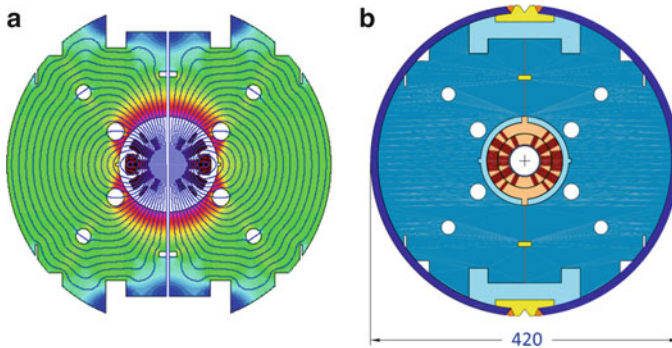


Fig. 7.2 Single-aperture dipole cross-section: (a) magnetic flux distribution and (b) mechanical structure

Table 7.2 Magnet design parameters

Parameter	Value
Transfer function (T/kA)	0.555
Current at 11 T in the bore (kA)	19.82
Stored energy at 11 T (kJ/m)	241
Magnet inductance (mH/m)	1.50
Total cable area (mm ²)	2461

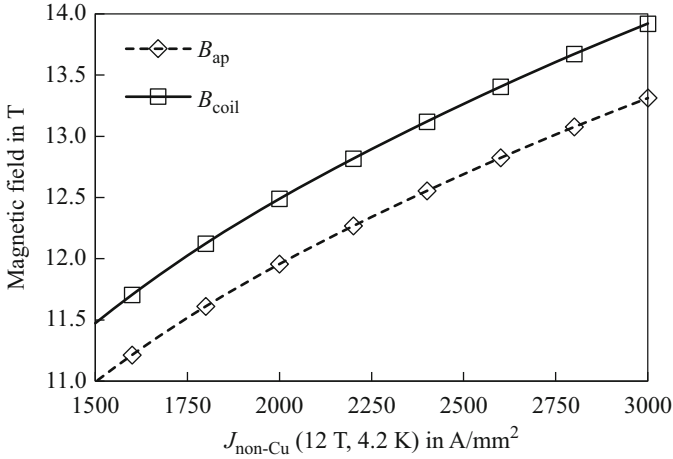


Fig. 7.3 Peak coil and bore fields vs. wire $J_c(12 \text{ T}, 4.2 \text{ K})$

The calculated values of the coil peak field and the magnet bore field at quench vs. the critical current density $J_c(12 \text{ T}, 4.2 \text{ K})$ of Nb_3Sn cable are shown in Fig. 7.3. To reach a bore field of 11 T the critical current density of round wires at 12 T and 4.2 K has to be 1650 A/mm^2 , assuming 10% of critical current degradation during cabling.

7.3.1.1 Magnetic Analysis

The field in the magnet aperture is represented in terms of harmonic coefficients defined by

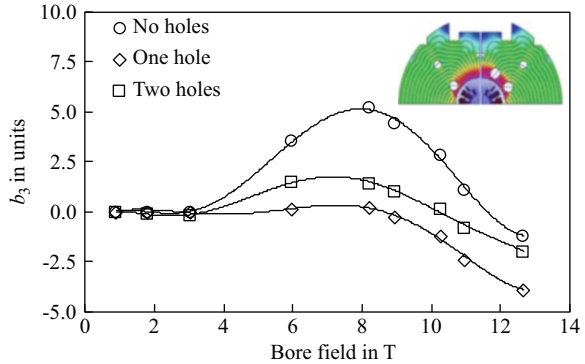
$$B_y + iB_x = B_1 \sum_{n=1}^{\infty} (b_n + ia_n) \left(\frac{x + iy}{R_{\text{ref}}} \right)^{n-1},$$

where B_x and B_y are the horizontal and vertical transverse field components, B_1 is the dipole field component, and b_n and a_n are the $2n$ -pole coefficients at a reference radius $R_{\text{ref}} = 10 \text{ mm}$.

Due to the coil cross-section optimization the low-order geometrical harmonics are small, less than 10^{-5} of the main dipole field (0.1 unit). The calculated effect of iron saturation on field quality is shown in Fig. 7.4. For the yoke without special correction holes the b_3 variations are within 7 units, reaching a maximum at $\sim 8 \text{ T}$. It was found that adding one or two correction holes decreases this effect below 2 units for bore fields up to 11 T (Ambrosio et al. 2000b). The iron saturation effect on higher order harmonics is small.

Analysis shows that the coil magnetization effect at low fields in Nb_3Sn magnets is large. For the Nb_3Sn wires available at the time, with an effective filament

Fig. 7.4 Effect of iron saturation on the sextupole field component b_3 with and without correction holes. (Ambrosio et al. 2000d)



diameter D_{eff} of ~ 0.10 mm, b_3 in the magnet aperture at 1 T reaches -25 units. Some decrease of this effect was expected by reducing the D_{eff} in Nb₃Sn wires. The eddy current effects were expected to be suppressed by using Nb₃Sn wires with a small twist pitch and cables with a resistive inter-layer core.

7.3.1.2 Mechanical Analysis

A finite element analysis (FEA) using ANSYS software (ANSYS Inc., Canonsburg, PA) was performed to optimize the coil stress during magnet assembly and operation, and to evaluate the maximum stresses in key elements of the magnet support structure (Ambrosio et al. 2000c). The results are summarized in Table 7.3.

After clamping and skin welding at room temperature, the area with a highest stress of 80 MPa is at the inner radius of the coil inner layer near the pole wedge. The clamps provide $\sim 40\%$ of the total coil pre-stress during magnet assembly. The coil bore is almost round with a difference of less than 0.004 mm along the horizontal and vertical radii.

At liquid helium temperatures, the stress distribution on the coil inner surface becomes non-uniform due to the coil horizontal deformation. The difference between the aperture horizontal and vertical radii increases to approximately 0.10 mm. The coil stress ranges from 121 MPa in the inner-layer pole turn to 11 MPa in the inner-layer mid-plane turn.

At the design field of 11 T the coil is still under compression and the maximum stress of 100 MPa is at the mid-plane of inner and outer layers. At 12 T the stress distribution is the same, although some small fractions of the coil-pole interfaces are under a small tension. The coil bore shape returns back to an approximate circle, with a difference along the horizontal and vertical radii of ~ 0.01 mm.

The data show that the magnet coil is under compression under all conditions, and that the maximum stress in the coil is always less than 125 MPa. The maximum stress in key elements of the magnet support structure is less than the material's yield stress. The shear stress on the major interfaces does not exceed 30 MPa. All these values are acceptable.

Table 7.3 Peak equivalent stress in coil and support structure

Stage	Peak equivalent stress (MPa)				
	Coil	Spacer	Yoke	Clamp	Skin
Assembly (300 K)	80	166	110	135	200
Cool-down (4.2 K)	121	125	110	124	330
Nominal field (11 T)	100	97	133	128	350

7.3.1.3 Quench Protection

Coil protection in case of a quench in accelerator magnets is typically provided by internal quench heaters (Ambrosio et al. 2000d). In a two-layer coil, quench heaters can be placed inside the thin inter-layer spacer, to quench practically all of the turns in both top and bottom coils, or on the coil outer layer. Analysis shows that in both cases quench heaters provide reliable magnet protection, ensuring a low coil temperature and low voltages.

7.3.2 Twin-Aperture Designs and Parameters

The Nb₃Sn coil described above was used to design twin-aperture dipoles for VLHC (Kashikhin and Zlobin 2001). The dipole cross-sections with cold and warm iron, and with horizontal and vertical arrangements of apertures are shown in Fig. 7.5.

In the design shown in Fig. 7.5a, the two coils are placed side by side inside a cold iron with an aperture separation of 180 mm. This distance can be varied within the 160–200 mm range for the same iron size without noticeable impact on the field quality. The iron is split into three pieces. The coil pre-stress and support is provided by clamped iron blocks and an external shell (also known as skin). Since the horizontal components of the Lorentz force between coils are compensated inside the iron, a 10 mm thick stainless-steel skin is adequate for coil support. An open vertical gap between the iron pieces minimizes the decrease of coil pre-stress after cool-down. To minimize the impact of gap size variations on field quality, the iron split is partially parallel to the magnetic flux lines. The iron saturation effect is suppressed by special holes and by optimizing the iron size.

In the design shown in Figs. 7.5c, d, the warm iron is sufficiently distanced from the coils to provide room for the cold mass support system, the thermal shield, and the vacuum vessel. The two coils are placed inside the iron with an aperture separation of 180 mm as in the design in Figs. 7.5a, b. The coil pre-stress and mechanical support is provided by thick aluminum rings, stainless-steel inserts and, if necessary, the cold mass skin. The iron inner radius and thickness were optimized considering field quality, fringe fields, iron cross-section, and the cryostat design requirements. This design allows for a significant reduction of magnet cross-section with respect to the cold iron design. The iron saturation effect in the warm iron design is small. Magnetic coupling between the two apertures, however, produces a

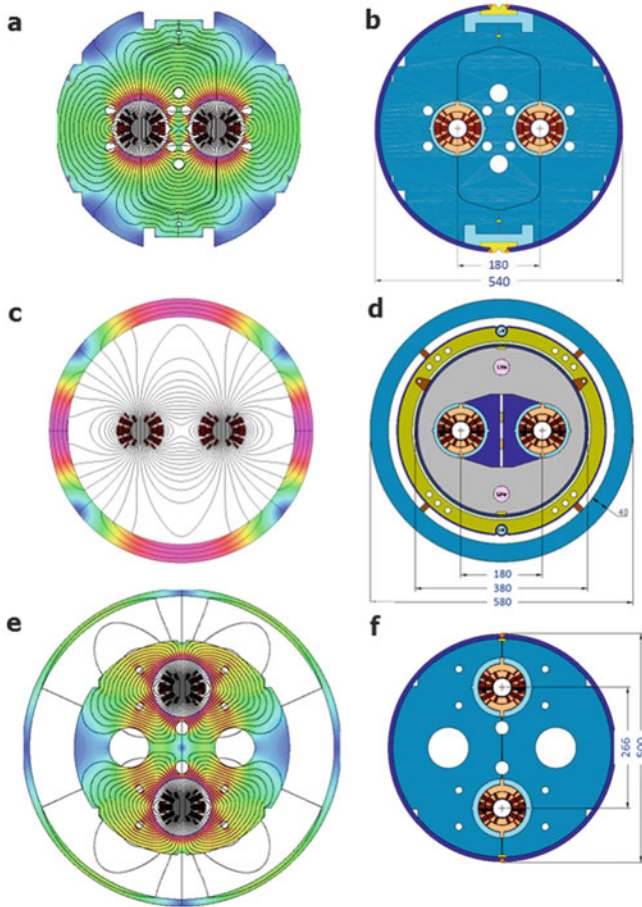


Fig. 7.5 Twin-aperture dipole magnets based on the cos-theta Nb₃Sn coil. (a, b, e, f) Cold; and (c, d) warm iron. (a, b, c, d) Horizontal; and (e, f) vertical bore arrangement. (Kashikhin and Zlobin 2001)

large quadrupole field component. It is cancelled in each aperture by the geometrical quadrupole component produced by the small left–right asymmetry in the coil block position. To reduce the force imbalance and the effect on the field quality, the warm iron design requires a proper alignment of the cold mass inside the iron. Analysis shows that these alignment requirements can be easily met.

In the design shown in Figs. 7.5e, f, the two coils are placed vertically inside the cold iron. To reduce the negative magnetic coupling, which reduces the dipole field in each aperture, the aperture separation should be at least 266 mm. To reduce the size of the cold mass, the iron is divided into two parts—cold and warm. The iron cold part is vertically split into two pieces for coil assembly and preload. To provide

an adequate coil pre-stress and support in this design, a 20 mm thick stainless-steel skin is needed. Since the horizontal components of the Lorentz force in each coil are added, the skin in this design is a factor of two thicker than in the design in Figs. 7.5a, b. To minimize the pre-stress decrease after cool-down, the cold iron gap remains open. The warm part of the iron is properly distanced to accommodate the cryostat elements as in the design in Figs. 7.5c, d. The iron saturation effect in this design is corrected by using holes in the cold iron, and optimizing the inner and outer radii of the cold and warm iron parts.

The mechanical analysis shows that in all the above designs the coil is under compression and the stress is always less than 150 MPa, which is acceptable for brittle Nb₃Sn cable. The coil bore deformations are less than 0.10 mm, and all structural elements work in elastic mode.

The main parameters of the dipole magnets described above are summarized in Table 7.4. The calculated geometrical harmonics are small; they are shown in Table 7.5.

The maximum bore field and quench current were calculated for Nb₃Sn wires with a Cu/non-Cu ratio of 0.85 and a critical current density $J_c(12\text{ T}, 4.2\text{ K})$ of 2 kA/mm² assuming a 10% critical current degradation due to wire plastic deformation during cabling. These designs could provide a nominal field of

Table 7.4 Calculated magnet parameters

	Bore arrangement		
	Horizontal		Vertical
Yoke design	Cold	Warm	Cold/warm
Magnet aperture (mm)	43.5	43.5	43.5
Aperture separation (mm)	180	180	266
Iron yoke diameter (mm)	520	580	564/710
Iron yoke area (cm ²)	1722	679	1378/327
Maximum bore field (T)	12.05	11.34	11.59
Maximum quench current (kA)	21.9	24.0	22.3
Stored energy at 11 T (kJ/m)	520	588	554
Inductance at 11 T (mH/m)	2.68	2.16	2.46

Table 7.5 Geometrical harmonics b_n at $R_{\text{ref}} = 10\text{ mm}$ (10^{-4})

Harmonic number	Horizontal		Vertical
	Cold yoke	Warm yoke	Cold yoke
2	–	0.000	–
3	0.000	0.000	0.000
4	–	0.000	–
5	0.000	0.001	–0.000
6	–	–0.012	–
7	0.000	–0.011	–0.006
8	–	0.031	–
9	–0.091	–0.130	–0.067

10–11 T with a margin within 10–15% using Nb₃Sn wires with $J_c(12\text{ T}, 4.2\text{ K})$ of 3 kA/mm² and a Cu/non-Cu ratio of 1.2 to ensure quench protection. Nb₃Sn composite wires with such a high J_c became available around 2005 from Oxford Superconductor Technologies (OST) (Parrell et al. 2005). Notice that the magnet design with a warm yoke allows for a substantial reduction in size without noticeable decrease in performance.

7.4 Fabrication Technology

Due to the small bending radii defined by the size of the inner-layer pole block, the coil manufacturing technology requires using the wind-and-react (W&R) method. In this approach the superconducting Nb₃Sn phase is formed after coil winding during its high temperature heat treatment.

The W&R technique imposes demanding requirements upon the coil components, which must survive a long heat treatment at a high temperature of ~700 °C, in the presence of thermo-mechanical stresses. Despite the relatively high cost, ceramic insulation was selected for the dipole models of this series. This insulation, developed by CTD in the late 1990s, did not use organic ingredients and showed excellent mechanical and electrical properties before and after the high-temperature heat treatment (Rice et al. 1999; Chichili et al. 2000). Alternative, less expensive S2-glass tape, traditionally used in Nb₃Sn magnets, was initially declined, primarily due to the presence of organic sizing, which involved additional processing. Later S2-glass tapes without organic components were successfully used in short and long coils of this series. To reinforce insulation after reaction, Nb₃Sn coils are impregnated with epoxy.

Cos-theta coils use complex 3D end parts. In the case of the W&R approach they also must withstand the coil heat treatment without noticeable deformations, which could cause shorts to the coils. An optimization method to design 3D metallic end parts was developed and successfully tested at FNAL (Yadav et al. 2001). Newly developed rapid prototyping techniques were used for the first time to reduce the time and cost of end part design. Emerging technologies, such as water-jet cutting, which reduced the end part fabrication cost by a factor of 2 and the processing time by a factor of 10, were also successfully used (Zlobin et al. 2005).

New features were introduced in the magnet fabrication process to simplify coil manufacturing and handling, and to reduce magnet production cost.

- To increase the cable mechanical stability and reduce the risk of turn-to-turn shorts during winding, the ceramic tape was impregnated with a liquid ceramic binder and pre-cured at 120 °C.
- To obtain a solid coil structure and the desired coil size, each coil layer was impregnated again after winding with a ceramic binder and cured at 120 °C in a precise mold.

- To reduce coil fabrication time and allow easy coil handling and warm field quality control before magnet assembly, two coils were assembled, reacted, and epoxy impregnated to form a thick, round, solid pipe.
- To reduce assembly time and costs, expensive collars and delicate and time-consuming collaring procedures were eliminated in this design. Later, safe collaring procedures for brittle Nb₃Sn coils were also developed and successfully demonstrated at FNAL (Bossert et al. 2010), and used in the 11 T dipole for the LHC upgrades (see Chap. 8).

The main steps of the developed coil fabrication technology, magnet assembly, and coil preload were verified using mechanical and technological models (Andreev et al. 2000; Chichili et al. 2001). This approach proved to be very useful in complicated accelerator magnet R&D programs.

7.4.1 Mechanical Model

A 200 mm long mechanical model was assembled and tested to verify the results of the magnet mechanical analysis and to choose the most appropriate coil shim plan. For this purpose a special coil was wound, cured, reacted, and epoxy impregnated. The Nb₃Sn cable for this coil was made from IT composite wire developed for the International Thermonuclear Experimental Reactor and insulated with S-2 glass. The coil straight section was cut into two halves, covered with spacers, and assembled inside the iron blocks. The assembly was clamped with aluminum clamps in a press and preloaded by a welded skin (Fig. 7.6). The mechanical model was heavily instrumented with strain gauges to monitor stress evolution during coil clamping, skin welding, and model cooling-down with liquid nitrogen to a temperature of 77 K.

Table 7.6 presents the strain gauge data at various stages of the model assembly. The experimental data are in good agreement with the FEA predictions shown in parentheses. The outer diameter of the epoxy impregnated coil “pipe” was 0.25 mm

Fig. 7.6 Instrumented short mechanical model.
(Andreev et al. 2000)



Table 7.6 Data from the mechanical model and FEA

	Coil	Spacer	
	Pole (MPa)	Mid-plane (MPa)	Pole (MPa)
Yoking in press	154 (145)	88 (122)	152 (156)
After spring-back	32 (40)	40 (43)	51 (50)
After skin welding	66 (72)	68 (65)	84 (81)
At 77 K	61 (73)	46 (45)	68 (56)

FEA predictions are shown in parentheses

larger than the nominal coil size, leading to high stresses in the coil during yoking in press. After spring-back, the stress in the coil decreased to ~32 MPa. The final coil pre-stress was provided by the skin through weld shrinkage, achieving the required pre-stress within 10%.

7.4.2 Technological Model (HFDA01)

The main goal of the 1 m long technological model was to check the tooling, optimize the coil fabrication and magnet assembly processes, and develop the instrumentation and quality control procedures. In the case of successful assembly, it was expected to proceed with cryogenic testing of this model.

7.4.2.1 Strand and Cable

The Rutherford cable used in this model had 28 strands, each of 1.0 mm diameter, a 0.025 mm thick stainless-steel core, a width of 14.23 mm, a mid-thickness of 1.82 mm, and a keystone angle of 0.927°. The cable was made at LBNL. The Nb₃Sn composite wire was produced by OST using the modified jelly roll (MJR) process. The round wire had a filament diameter of ~0.115 mm and a Cu/non-Cu ratio of 0.92. The measured critical current density at 12 T and 4.2 K for the round wire was ~2000 A/mm² and the RRR was ~30. The I_c degradation due to cabling, measured using round wires and extracted strands, was less than 10% for this cable, which had a quite large packing factor of 89%. The quality of the cable was not completely satisfactory. It was found that at several locations the core stuck between the strands, although it did not protrude out of the cable surface, except for one location.

The cable was cleaned with ABZOL VG solvent and wrapped with CTD-CF100 ceramic tape with a 50% overlap. The nominal thickness of the cable insulation was 0.25 mm. Inorganic CTD-1002x ceramic binder was applied to the insulated cable using rollers. The entire spool of wet insulated cable was cured at 80 °C for about 20 min to achieve a strong cable insulation system.

7.4.2.2 Coil Winding and Curing

Both coil layers were wound using a single cable piece. Coil end parts, wedges, and pole blocks were made of aluminum-silicon bronze C642. The end parts were fabricated at LBNL using five-axis computerized numerical control machining and coated with a 0.125 mm thick ceramic layer.

Small axial gaps were introduced between the pole blocks and between the wedges and end parts to account for differential thermal expansion during reaction in the axial direction. Voltage taps made of thin stainless-steel strips were inserted between the cable and the insulation during winding around the end parts. After the winding of the inner coil, the ceramic binder was applied and the wet coil was prepared for curing. After preliminary cycling at low pressures, a final azimuthal pressure of 45 MPa and a radial pressure of 10 MPa were applied to achieve the target coil geometry. The curing temperature of 150 °C was held for 30 min to provide good turn bonding.

The inter-layer insulation was made of three layers of 0.125 mm thick ceramic cloth. The middle layer contained two quench protection heaters made of 0.025 mm thick stainless-steel strips (Fig. 7.7). The insulation assembly was impregnated with ceramic binder and cured in a special fixture. The coil outer layer was wound on top of the cured inner layer, which was covered by the inter-layer insulation. The outer layer was then filled with ceramic binder and cured along with the previously cured inner layer. A cured coil for the technological model is shown in Fig. 7.8.

The azimuthal size of the cured coils was measured at four locations along the coil straight section at an azimuthal pressure of 2 MPa. The average azimuthal size for the first coil was 0.2 mm over its nominal size. To correct the coil size of the second coil, the wedge insulation was changed from 50% overlap to butt lap. The average azimuthal size of the second coil at 2 MPa was only 0.01 mm over the nominal coil size. The average measured azimuthal modulus of elasticity for the cured coils was about 20 GPa. Electrical measurements, taken on the coils to check for turn-to-turn shorts, did not detect any problems at that stage.



Fig. 7.7 The middle layer of the inter-layer insulation with strip-heaters. (Chichili et al. 2001)



Fig. 7.8 Dipole coil with coated parts after impregnation with ceramic binder and curing in a precise mold. (Chichili et al. 2001)

7.4.2.3 Coil Reaction

Two coils with ground insulation were mounted around a stainless-steel mandrel and placed in the reaction fixture. The ground insulation consisted of three layers of 0.125 mm thick ceramic cloth preformed into shape using the ceramic binder. The cable ends were welded to prevent tin leakage during reaction. The retort was pumped for several hours and then purged with argon with a flow rate of $\sim 1 \text{ cm}^3/\text{s}$. The reaction cycle had two steps: $575 \text{ }^\circ\text{C}$ for 200 h followed by $700 \text{ }^\circ\text{C}$ for 40 h with a ramp rate of $25 \text{ }^\circ\text{C}/\text{h}$. The coil temperature was monitored at several locations throughout the reaction. The difference between the coil and the furnace temperature above $500 \text{ }^\circ\text{C}$ was less than $2 \text{ }^\circ\text{C}$.

Both mechanical and electrical measurements were also taken on the coils after reaction. It was found that after reaction the coils expanded axially by 9 mm (!) whereas the length of an annealed MJR cable in free state expanded by only 1 mm/m. This unexpectedly large increase of the coil length was related to the restricted radial and free axial coil expansion in the reaction fixture.

The azimuthal coil size was measured using a reacted practice coil. It was found that it increased after reaction by about 0.5 mm at an applied pressure of $\sim 15 \text{ MPa}$. Therefore, the size of the next coils during curing was reduced by 0.5 mm to allow the coils to grow azimuthally to the nominal size during reaction, thereby avoiding high pressure in the mold and coil axial extrusion.

Tin leaks were found in both coils after reaction. This defect was attributed to the lack of a low temperature step at $200\text{--}210 \text{ }^\circ\text{C}$, when tin diffuses as a solid phase, as well as to the high coil compression during reaction. Even though the coils were clearly damaged, magnet fabrication was continued to study all aspects of the assembly procedure.

7.4.2.4 Splice Joints

Brittle Nb_3Sn coil leads were spliced to flexible Nb-Ti cables using special tooling and Pb-30Sn solder with Kester 44 Rosin Flux. Splicing was performed while coils were still inside the reaction fixture. Each Nb_3Sn lead was placed between two Nb-Ti cables and encased in a 0.55 mm thick, 125 mm long copper cage with a copper top plate. The Nb_3Sn leads and the Nb-Ti cables were always supported to protect the brittle Nb_3Sn cable from any possible damage. Both splice joints were heated to $\sim 230^\circ\text{C}$ by heaters placed in tooling slots. The bolts on the tooling were tightened with the increase in temperature until the right splice geometry was obtained.

7.4.2.5 Epoxy Impregnation

Two coils were impregnated together with CTD-101K epoxy at a temperature of 60°C . The stainless-steel mandrel used during reaction was replaced with a Teflon mandrel. The mandrel diameter was chosen such that at the curing temperature it expanded to fill the coil aperture. Thanks to the large thermal expansion of Teflon, after impregnation it was easily removed from the coil aperture. A 0.125 mm thick mold-released polyimide film was placed between and around the coils in the impregnation fixture. In principle, this polyimide layer allowed splitting the coils after impregnation. Pictures of impregnated coils are shown in Fig. 7.9.

7.4.2.6 Model Assembly and Instrumentation

The impregnated coil assembly and various components of the magnet support structure were instrumented with gauges to measure stress values during magnet assembly and operation. To measure the azimuthal stress, four capacitance gauges were installed between the outer pole blocks and the coil. Capacitance gauges were

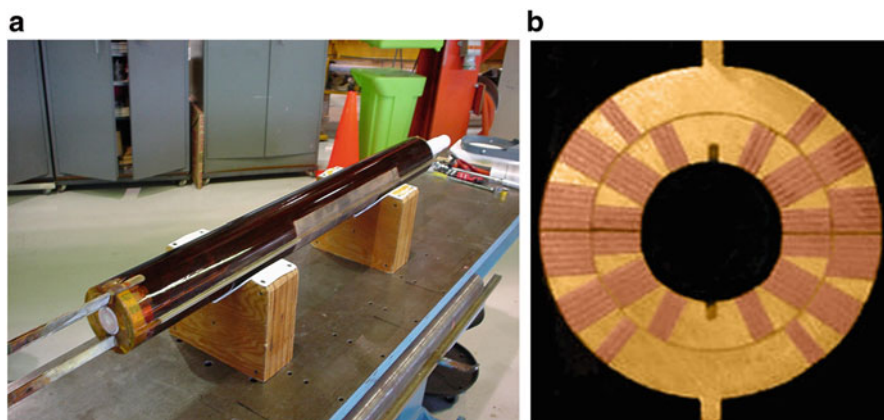


Fig. 7.9 (a) Epoxy impregnated coil assembly with Teflon mandrel in the aperture; and (b) cross-section of the impregnated coil. (Chichili et al. 2001)



Fig. 7.10 Coil-yoke assembly inside the yoking and clamping tooling ready for installation in the vertical press. (Chichili et al. 2001)

fabricated in-house and calibrated at room and helium temperatures. Resistive strain gauges were installed on spacers, clamps, and the skin.

The coils and yoke were assembled in a dedicated tooling and then compressed in a vertical press (Fig. 7.10). The press load was increased incrementally until the gap between the yoke halves, which was controlled by dial indicators, reached the nominal value. At this pressure the aluminum clamps were easily inserted using a separate set of pusher blocks. Then, the press load was released and the assembly sprang back to an equilibrium position. The measured maximum stress in the pole region of the coil outer layer was about 100 MPa, while the stress in the coil–yoke spacers was 200 MPa in the pole region and 100 MPa in the spacer mid-plane.

At this stage the assembly of the technological model was complete. Lessons learned during coil fabrication and magnet assembly were implemented in the next dipole models.

7.5 Short Models

7.5.1 Short Dipole Models

Six 1 m long dipole models of the HFDA series were fabricated and tested at FNAL from 2001 to 2005. The first three models, HFDA02 to HFDA04, used cables made from MJR Nb₃Sn composite wire produced by OST. The next three models,

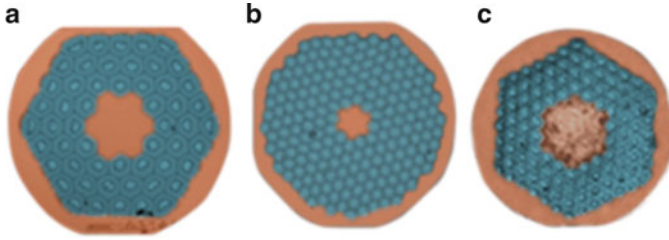


Fig. 7.11 Cross-sections of Nb₃Sn round wires: (a) MJR54/61; (b) PIT192; and (c) RRP108/127. (Zlobin 2011)

HFDA05 to HFDA07, used cables made from powder-in-tube (PIT) Nb₃Sn wire produced by Shape Metal Innovation. The MJR round wire had a higher critical current density $J_c(12\text{ T}, 4.2\text{ K})$ of 2.0–2.2 kA/mm², but a larger sub-element diameter D_{eff} of ~0.100 mm, whereas the PIT round wire had a lower J_c of ~1.6–1.8 kA/mm² and a smaller D_{eff} of ~0.050 mm.

In the early 2000s, a new improved R&D composite wire based on the restack rod process (RRP) was developed by OST (Parrell et al. 2005). This wire had a high $J_c(12\text{ T}, 4.2\text{ K})$ up to 3 kA/mm², and a larger number of smaller sub-elements, which significantly improved the stability of this wire with respect to “flux jumps.” The cross-sections of the round Nb₃Sn wires used in the HFDA dipole models are shown in Fig. 7.11.

The cable in HFDA01 to HFDA03 had a 0.025 mm thick stainless-steel core to control the inter-strand resistance, while the cable in HFDA04 to HFDA07 had no core. Cables used in HFDA01–05 had 28 strands; the number of strand was then reduced to 27 to optimize the cable packing factor. Cross-sections of the 28-strand and 27-strand Rutherford cables without core made from PIT composite wire are shown in Fig. 7.12.

The cable for the first eleven 1 m long coils was produced at LBNL. The cable for 1 m long coils 12–19, for the 2 m long coil 20, and for the 4 m long coil 21 was made in-house using FNAL cabling machine. The cable for coils 1–11 was cleaned with ABZOL VG to remove any oil residue left from the cabling process. Later, it was found that cable cleaning does not affect coil properties, thus cable cleaning for the subsequent coils was not used.

The main features of the 1 m long dipole models HFDA02–07 are summarized in Table 7.7. The magnet design and fabrication procedures were similar to those used in the technological model HFDA01. Some design and technological changes were introduced throughout the short model R&D to address the problems found during the technological model fabrication, and to incorporate the feedback from dipole model fabrication and tests. The most important changes are described below.

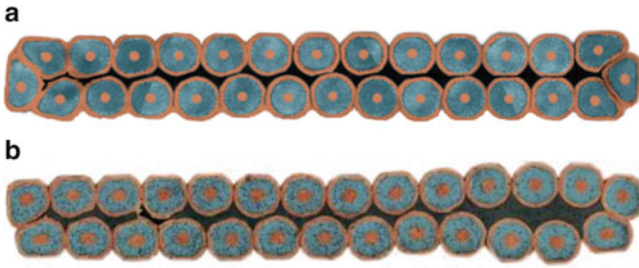


Fig. 7.12 Cross-sections of (a) 28-strand and (b) 27-strand cables

Table 7.7 HFDA model features

Magnet HFDA	Coil number	Strand type	Cable core	Coil ends	Coil impregnation	Skin design
02	3, 4	MJR	Yes	v. 1	Glued	Welded
03	5, 6	MJR	Yes	v. 1	Glued	Welded
04	7, 8	MJR	No	v. 2	Glued	Welded
05	12, 13	PIT	No	v. 2	Separate	Bolted
06	14, 15	PIT	No	v. 2	Separate	Bolted
07	12, 14	PIT	No	v. 2	Separate	Bolted

7.5.1.1 HFDA02

The cable insulation had 30% overlap in coil 3 and 40% in coil 4. The coil azimuthal size during curing was reduced by 0.5 mm with respect to the nominal coil size, such that after reaction the coils were at the nominal size without excessive pressure on the conductor during reaction. Coil 3 was about 0.2 mm larger than coil 4 due to the difference in mid-thickness of the used bare cable.

The coil end parts (v. 2) were re-optimized to better match the cable positions in the end areas (Fig. 7.13). The end parts were produced using water-jet machining, which is more cost-effective than five-axis CNC machining. No end-part coating was used in this and the following magnets.

The coil reaction cycle was revised to avoid the tin leaks observed in the technological model coils. The new heat treatment cycle included three steps: 210 °C for 100 h, 340 °C for 48 h, and 650 °C for 180 h. This heat treatment schedule was used for all the short models made of the MJR cables.

Ground insulation was made of two layers of 0.25 mm thick ceramic cloth. Since it was found that the heater strips between the two coil layers in the technological model had been jammed during coil processing, which increased the risk of heater-to-coil shorts, quench protection heaters in this and the next models of this series were installed between the two layers of ground insulation. Voltage taps were installed only on the coil leads.

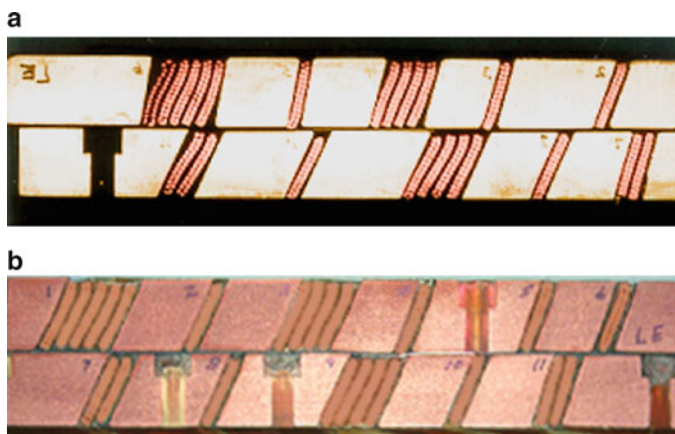


Fig. 7.13 Longitudinal sections of the coil lead end with (a) first; and (b) second generation end parts

7.5.1.2 HFDA03

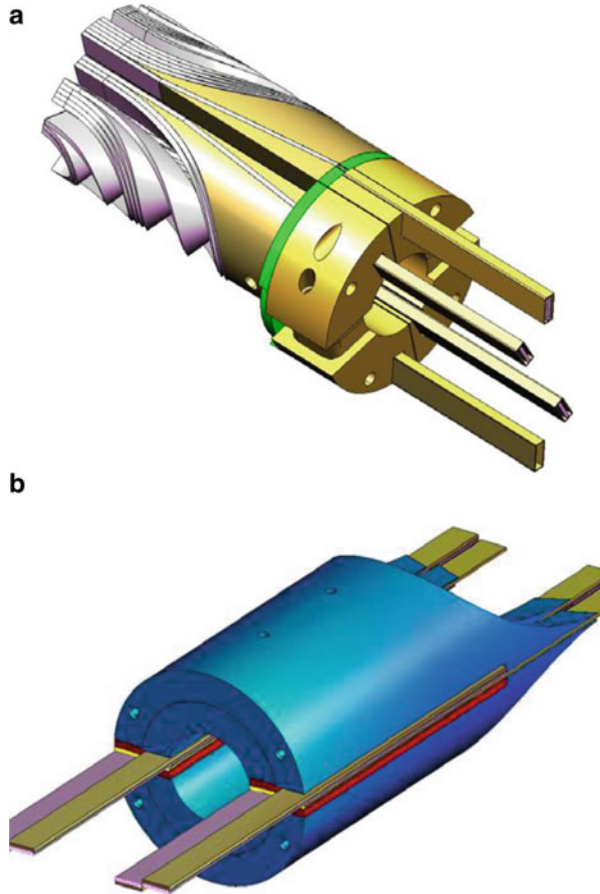
The HFDA03 fabrication process was similar to that of HFDA02. The two coils in this magnet had virtually the same azimuthal size. To provide more flexibility in adjusting the tooling and to improve splice quality, a new splicing fixture was made to splice each Nb_3Sn lead individually. The splicing procedure was adjusted to eliminate possible strand damage, which was believed to be one of the main reasons for the poor quench performance of HFDA02. To provide visual control of the splice quality, copper boxes were not used.

The ground insulation consisted of three layers of 0.125 mm thick ceramic cloth. Strip heaters were weaved (see Fig. 7.7) into the insulation middle layer. Additional voltage taps were placed on the outer layer of each coil, adjacent to the layer jump. Special holes were made in the iron yoke to correct the iron saturation effect in the normal sextupole b_3 . This iron yoke was used for all following dipole models.

7.5.1.3 HFDA04

Based on the HFDA03 test results, the coil lead end was redesigned to keep the coil lead cables in the mid-plane (Fig. 7.14). The entire splice joint was placed in the lead end saddle to ensure reliable splice support during splicing and at all stages of magnet assembly and operation. The length of the coil straight section in this and the next short models was reduced by ~ 200 mm to house the lead splices within the coil end saddle and still use the same tooling. To allow better control of the coil mid-plane position and provide the possibility of splicing each coil lead individually, the two coils were separated in the reaction fixture by a stainless-steel plate.

Fig. 7.14 Coil end design: (a) version 1; and (b) version 2 with straight coil leads



Coil 7 was impregnated first alone, and then coil 8 was impregnated together with coil 7. The first step ensured an accurate mid-plane position and the second step provided proper matching of the two coils in the mid-plane areas.

Coil alignment inside the iron yoke was done using only one outer pole block with an extension. Special spacers were used to prevent large variations of the azimuthal stress in the left and right sides of the coil during yoking. The stainless-steel end blocks extended to cover part of the splice block, thus moving the stress discontinuity away from the Nb₃Sn lead.

HFDA04 was the last model that used the cable with MJR strands. By that time, it had been recognized and experimentally confirmed that strong flux jump instabilities in these strands with a large Nb₃Sn sub-element size were the main cause of the poor quench performance of HFDA02–04 (Zlobin et al. 2005).

7.5.1.4 HFDA05

The HFDA05 dipole was similar to HFDA04, except for the cable, which was made of PIT Nb₃Sn composite wires. Before insulation, the cable was annealed at 200 °C for 30 min to reduce residual stresses accumulated during cable manufacturing. The cable was insulated using a new insulation type. It was wrapped with two layers of 0.125 mm thick ceramic tape. The first layer was dry ceramic tape wrapped with a 0.75 mm gap. The second layer consisted of the same ceramic tape impregnated by the manufacturer with CTD-1008 binder. It was also wrapped with 0.75 mm gaps overlapping the gaps from the first layer.

The reaction cycle was adapted for the PIT wire and had only one step with a temperature ramp rate of 25 °C/h to a reaction temperature of 655 °C for 170 h. Both coils were reacted and impregnated separately to allow testing of the first PIT coil in a dipole mirror structure (see Sect. 7.5.1.7).

None of the outer pole blocks had alignment extensions. The coil alignment inside the yoke was done by using “scale” measurements. To eliminate large differences in azimuthal stress between the left and right sides of the coil assembly, special spacers were used, as in HFDA04. Unlike previous HFDA models, the HFDA05 yoke gap was, by design, closed after cool-down.

7.5.1.5 HFDA06

The cable type and preparation procedures were the same as in HFDA05. The cable was wrapped with 0.75 mm gaps with two layers of 0.125 mm thick and 12 mm wide ceramic tape pre-impregnated with binder. The outer layer was wrapped to overlap the gaps in the inner layer.

Each coil was impregnated with binder and cured in a closed cavity mold at 150 °C for 0.5 h with a 0.125 mm azimuthal polyimide shim in the mid-plane.

Coils 14 and 15 were reacted individually in a single-coil reaction fixture. The intended reaction cycle for both coils had three steps: 210 °C for 100 h, 331 °C for 48 h, and 675 °C for 64 h (coil 14) or 100 h (coil 15). The reaction of coil 14 was interrupted during ramping at 331 °C and then restarted several times due to malfunctioning of the oven. Nonetheless, coil 14 was the best performing PIT coil. Coils 14 and 15 were impregnated with epoxy separately after splicing with Nb-Ti leads in the same fixture that was used for reaction.

7.5.1.6 HFDA07

This magnet was assembled using the best coils, 12 and 14, previously tested in HFDA05 and HFDA06.

7.5.1.7 Dipole Mirror Magnets

Single dipole coils were tested using a special coil test structure (CTS), also known as dipole mirror, under operating conditions similar to those of real magnets (Chichili et al. 2004). CTS noticeably reduced the turnaround time of coil fabrication and evaluation, as well as material and labor costs. The dipole mirror used the same mechanical structures and assembly procedures as the complete dipole magnets, and allowed advanced instrumentation to be used.

The HFDM dipole mirror is shown in Fig. 7.15. The mirror's mechanical structure is similar to the HFDA dipole structure, except for the iron yoke, which is split horizontally, and one of the two coils is substituted with half-cylinder iron blocks. The transverse coil pre-stress and support are provided in the same way as in the dipoles by a combination of aluminum clamps and a bolted stainless-steel skin.

The main parameters of the coils tested in the dipole mirror structure are summarized in Table 7.8. The most important details of the mirror magnets are described below.

7.5.1.8 HFDM01

The first mirror magnet HFDM01A (also called HFDA03A) had two main goals—to test a mirror magnet structure with bolted skin, and to study the effect of lead splices on the magnet quench performance. The magnet used coil 5, which was tested previously in HFDA03. The goal of the HFDM01B test (also called HFDA03B) was to assess the splice joints in a configuration similar to a real magnet, because the

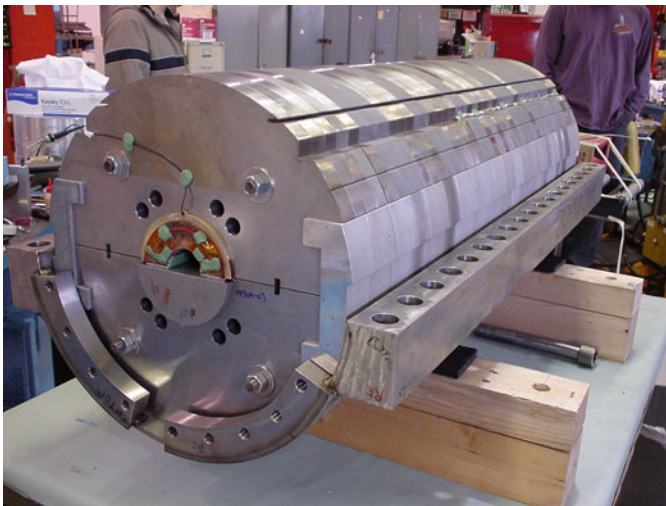


Fig. 7.15 Return end of short dipole mirror structure. The coil is paired with an iron semi-cylinder inside the iron yoke and the bolted skin half-shell. (Zlobin 2011)

Table 7.8 Dipole mirror design features

Mirror magnet	Coil number	Coil length (m)	Wire type	Wire diameter (mm)	Skin type
HFDM01	5	1	MJR54/61	1	Bolted
HFDM02	10	1	MJR54/61	1	Bolted
HFDM03	12	1	PIT192	1	Bolted
HFDM04	16	1	RRP54/61	0.7	Bolted
HFDM05	17	1	RRP54/61	0.7	Bolted
HFDM06	19	1	RRP108/127	1	Bolted
LM01	20	2	PIT192	1	Welded
LM02	21	4	RRP108/127	1	Welded

splices were initially suspected as the main cause of poor quench performance of the first HFDA dipole models. Additionally, HFDM01B allowed checking whether the conductor could carry currents above 20 kA under conditions similar to those found in a magnet. For this purpose, the inner- and outer-layer mid-plane turns on each side of coil 5 were cut from the rest of the coil, spliced to flexible Nb-Ti cables, and connected in series.

7.5.1.9 HFDM02

HFDM02 was fabricated and tested with a new coil 10, made from 28-strand MJR cable. The cable was insulated for the first time with pre-impregnated ceramic tape, which would later be used in HFDA05–07. Each end saddle had holes underneath the lead splice joints to improve splice cooling. The coil was reacted without the inner mandrel to allow for cable expansion inside the bore. This approach was chosen to reduce possible cable stress/strain degradation during reaction and improve gas removal from the coil before and during reaction. This trial coil demonstrated poor quench performance similarly to previously tested MJR coils. Therefore, it was not used in the next HFDA magnets.

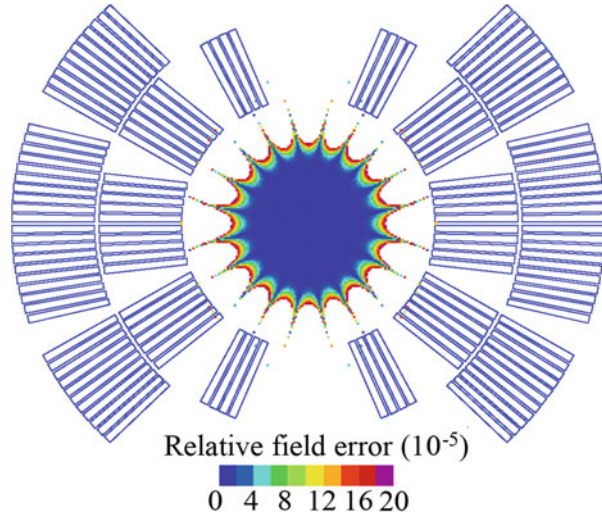
7.5.1.10 HFDM03

Coil 12, the first coil made of PIT cable, was tested first in a dipole mirror configuration to verify the effect of cable stability on the magnet performance. For the coil design and fabrication features, see HFDA05 described above.

7.5.1.11 HFDM04, HFDM05

These two mirror magnets were fabricated and tested to increase the dipole field to 11–12 T by using the newly developed high- J_c RRP strands. The cable had 39 strands, each of 0.7 mm diameter, a width of 14.34 mm, a mid-thickness of

Fig. 7.16 Coil cross-section based on 39-strand cable



1.258 mm, and a keystone angle of 0.972° . The cable for HFDM04 was produced at LBNL. The cable for HFDM05 was made in two steps. First, the rectangular cable was made at LBNL. Then it was annealed and re-rolled to its final keystone geometry at FNAL. A high- J_c 0.7 mm diameter RRP54/61 strand with a sub-element size of ~ 0.085 mm was used to mitigate the instability problems and thereby increase the achievable field. The coil cross-section was modified for this thinner 39-strand cable without changing the coil layer width and outer coil radius (Fig. 7.16). Three coils of this design were fabricated and two were tested in a mirror configuration.

7.5.1.12 HFDM06

This mirror magnet used the coil made of RRP108/127 Nb₃Sn strand 1 mm in diameter with a larger number of sub-elements and increased sub-element spacing. To reduce the strand deformation on the cable edges, the number of strands in the cable was reduced from 28 to 27. The Rutherford cable was made at FNAL in two steps. First a low-compaction rectangular cable was produced, and it was then re-rolled to its final keystone cross-section, after a short intermediate annealing of the rectangular cable at 190°C in air.

7.5.1.13 LM1 (HFDM07)

This mirror magnet was used to test the first 2 m long coil 12, which was made of 27-strand PIT cable. The coil fabrication procedure was similar to coils 14 and 15. The magnet assembly was similar to HFDM03.

7.5.1.14 LM2 (HFDM08)

This mirror magnet was used to test the first 4 m long Nb_3Sn dipole coil as part of the Nb_3Sn coil technology scale-up program. The coil was made of 27-strand Rutherford cable with 1 mm Nb_3Sn RRP108/127 strands. The total cable length in the coil was about 166 m. The coil design and the magnet fabrication procedure were similar to HFDM06.

7.6 Dipole Model Tests

Six short dipoles of the HFDA series were built and tested at FNAL from 2002 to 2006. It was the first in the world series of nearly identical Nb_3Sn accelerator magnets, which provided the first data on magnet quench performance, field quality, and especially on the reproducibility of magnet technology and performance.

7.6.1 Quench Performance

The HFDA dipole models were tested in liquid helium at 4.5 K and at lower temperatures. Quench performance of HFDA02 to HFDA07 is shown in Fig. 7.17. The first three models HFDA02 to HFDA04, made of the MJR wire, were limited by

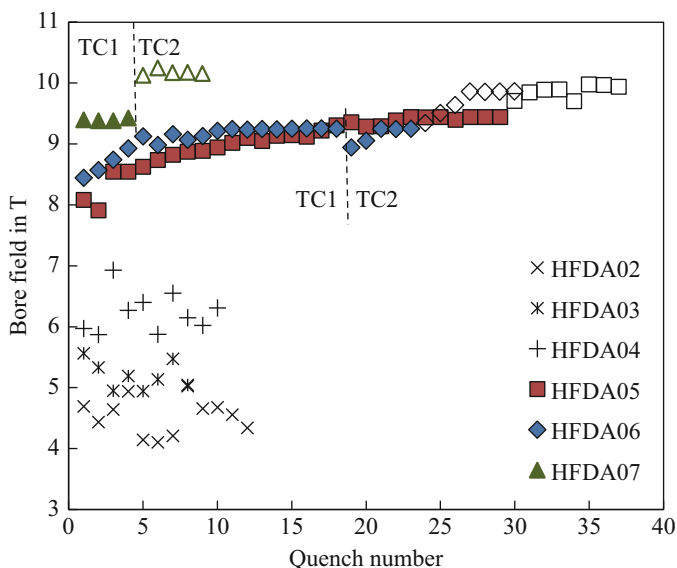


Fig. 7.17 HFDA02–07 training at 4.5 K (solid markers) and 2.2 K (open markers). TC1/TC2 represents thermal cycles

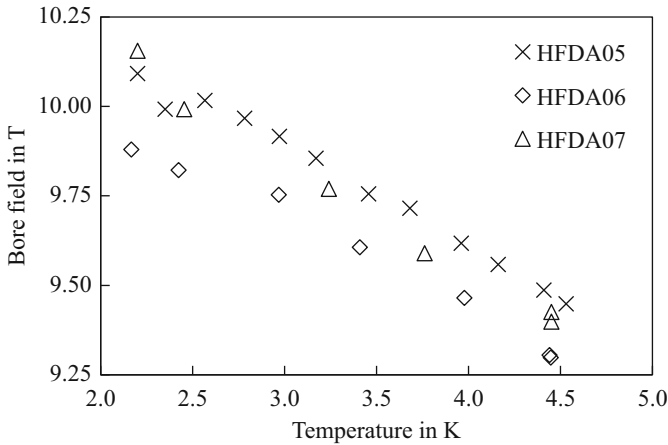


Fig. 7.18 Maximum bore field vs. coil temperature

flux jumps in the superconductor and only reached 4–7 T (Zlobin et al. 2005). The three last magnets were made of the more stable PIT wire, and at 4.5 K reached their short sample field of 9.3–9.4 T. The field level in these models was limited by the relatively low J_c of the PIT wire. At 2.2 K, the maximum field in PIT models increased to ~ 10 T thanks to the increase of the superconductor J_c at lower temperatures (Fig. 7.18).

Ramp rate dependences of the HFDA05–07 quench field normalized to the B_{\max} value measured at 4.5 K and $dI/dt = 20$ A/s are shown in Fig. 7.19. The shape of the ramp rate dependences at current ramp rates above 125–150 A/s suggests that they are dominated by the large eddy current losses in the cable without a stainless-steel core.

7.6.2 Field Quality

The field harmonics were measured at 4.5 K using a 250 mm long (43 mm long in HFDA05) 25 mm diameter probe. The probe had a tangential coil to measure high-order harmonics, as well as dedicated dipole and quadrupole coils to measure low order harmonics.

The transfer function TF, normal sextupole b_3 and decapole b_5 harmonics measured in HFDA07 vs. the bore field are shown in Fig. 7.20.

Analysis shows that the iron saturation effect in the TF is in a good agreement with the calculations. In b_3 the iron saturation effect was minimized at high fields by using special correction holes in the yoke.

Figure 7.21 shows the measured ramp rate sensitivity of the normal sextupole b_3 in HFDA02–07. In this figure the width Δb_3 of the sextupole loop at $B = 2$ T is plotted vs. the current ramp rate (Zlobin et al. 2007). HFDA02 to HFDA04 models

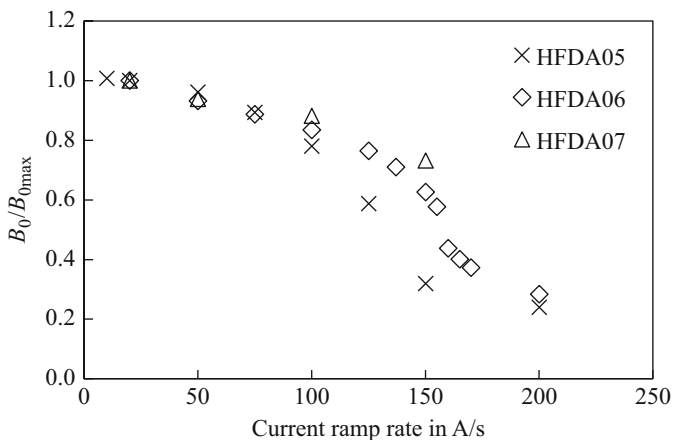


Fig. 7.19 Ramp rate sensitivity of magnet quench field

demonstrated a very small and reproducible eddy current effect, due to large crossover resistances in the cable with stainless-steel core and due to the high resistance of the strand matrix (RRR ~ 10). The Δb_3 in HFDA05 to HFDA07 rapidly changed with the ramp rate. The negative slope of the Δb_3 ramp rate dependences indicates that the effect was due to the eddy currents in the cable rather than in the strands in spite of the lower copper matrix resistivity in the PIT wires (RRR ~ 50). These results prove that the eddy current magnetization effect could be suppressed using cored cables and strands with a small twist pitch.

The width of sextupole loops Δb_3 extrapolated to $dI/dt = 0$ corresponds to the persistent current component of a coil magnetization, which is proportional to $J_c \cdot D_{\text{eff}}$. The persistent current effect is reproducible in HFDA models made of the same wire type. The b_3 loops in HFDA02 to HFDA04 were larger than in HFDA05 to HFDA07 due to the higher J_c and larger D_{eff} in the MJR wires. These larger values also caused noticeable b_3 fluctuations at low fields in these models, associated with flux jumps in the superconductor (Zlobin et al. 2006). It was realized that the large persistent current effect in Nb_3Sn accelerator magnets cannot be reduced to an acceptable level by reducing the sub-element size because of technological limitations for high- J_c Nb_3Sn wires based on the IT or PIT processes. It was shown, however, that the main component can be compensated using a simple passive correction based on thin iron strips developed and tested at FNAL (Kashikhin et al. 2003).

Measurements of b_3 decay and “snap-back” effects, important for accelerator magnets, were done at a 3 kA plateau for 30 min. It was found that the b_3 decay was very small relative to that seen in Nb-Ti accelerator magnets.

Geometrical field harmonics in HFDA02 to HFDA07 are shown in Table 7.9. They were determined as average values between current up and down ramps at 3 kA. The average values of the low-order geometrical harmonics for HFDA series

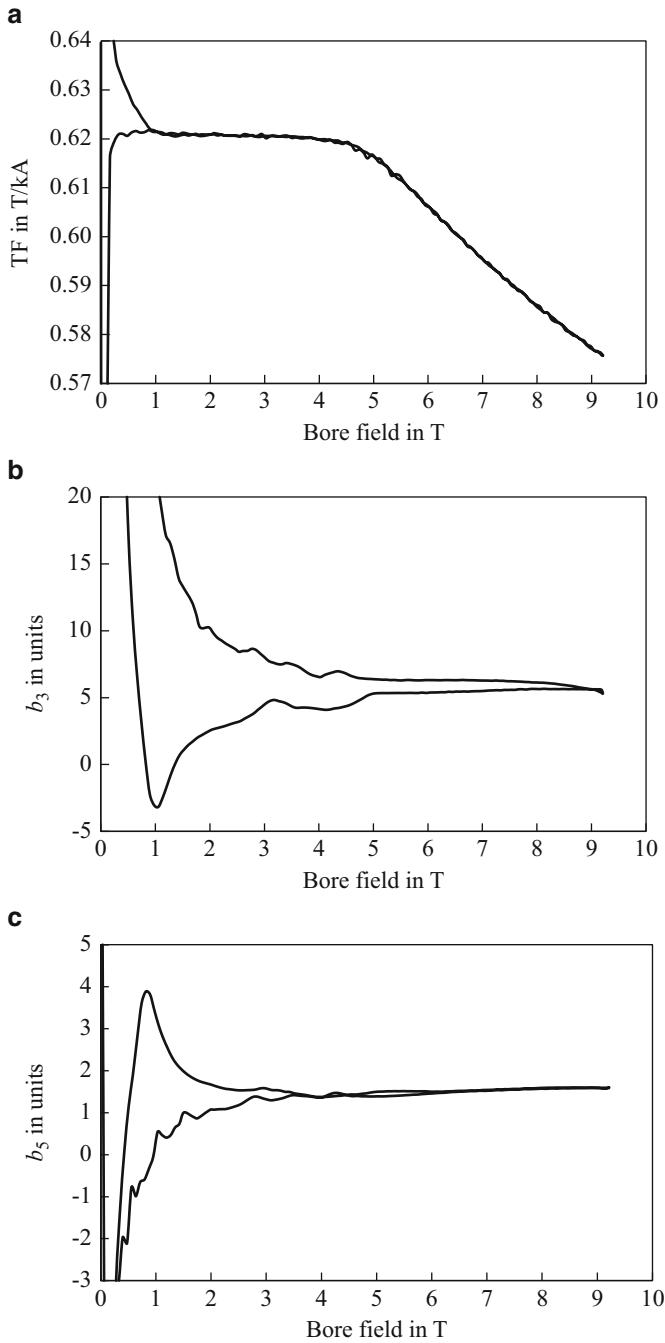


Fig. 7.20 Measured: (a) transfer function; (b) b_3 ; and (c) b_5 in HFDA07 vs. bore field

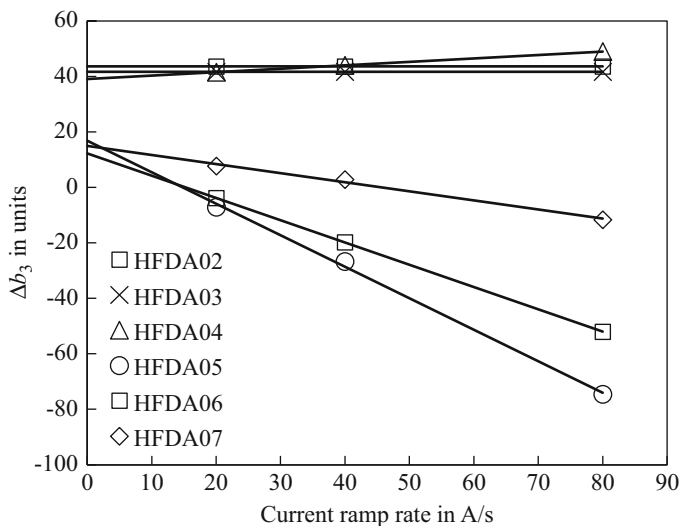


Fig. 7.21 Ramp rate sensitivity of the normal sextupole b_3 . (Zlobin et al. 2007)

Table 7.9 HFDA02–07 geometrical field harmonics, 10^{-4}

n	HFDA				SSC-40 mm	
	Average		SD		SD	
	a_n	b_n	a_n	b_n	a_n	b_n
2	-0.37	-0.15	7.3	4.1	2.77	0.79
3	0.55	2.06	0.6	4.3	0.22	1.24
4	-0.73	-0.06	0.9	0.7	0.29	0.15
5	0.17	0.60	0.1	0.9	0.12	0.30
6	-0.04	0.00	0.2	0.2	0.11	0.03
7	0.01	0.20	0.1	0.2	0.03	0.06
9	-0.02	-0.05	0.1	0.1	0.08	0.05

are rather small, below one unit, except for the normal sextupole b_3 . Standard deviations (SD) of the measured normal b_2 and skew a_2 gradients, and the normal b_3 sextupole, are relatively large with respect to the other harmonics.

The standard deviations of normal and skew harmonics measured in six HFDA models are compared in Table 7.9 with the results of the first six 40 mm aperture SSC dipole models made with Nb-Ti superconductor (Jackson 1986). The variation of skew harmonics in the Nb₃Sn and Nb-Ti models is rather close. The variation of normal harmonics is larger in the former, since it includes both fabrication errors of coil components and size variations of the shims used to adjust the coil pre-stress.

7.7 Dipole Mirror Tests

7.7.1 Conductor and Coil Technology Study

Six short dipole mirror magnets of the HFDM series were built and tested at FNAL between 2002 and 2006. The first tests were performed to validate the mirror structure and to develop and demonstrate the coil technology (HFDM01–02). Then the focus moved towards understanding and improving conductor and magnet flux jump stability (HFDM03–06).

Training data of dipole coils tested using the dipole mirror structure are plotted in Fig. 7.22. The coils made of 1 mm MJR54/61 wire with the largest D_{eff} , and those made with the first high- J_c 0.7 mm RRP54/61 wire with relatively low RRR demonstrated erratic quench performance and large quench current degradation at 4.5 K, as the corresponding dipole models. The coil made of 1 mm PIT192 wire showed stable training performance and reached its short sample limit (SSL) at 4.5 K. A similar performance was later confirmed by the PIT dipole models (Fig. 7.17). The coil with the high- J_c 1 mm RRP108/127 wire reached at 4.5 K the highest quench current, which corresponds to $\sim 97\%$ of its SSL limit. Noticeable variations of quench current at the current plateau, however, pointed to magnetic or, perhaps, mechanical instabilities in the coil.

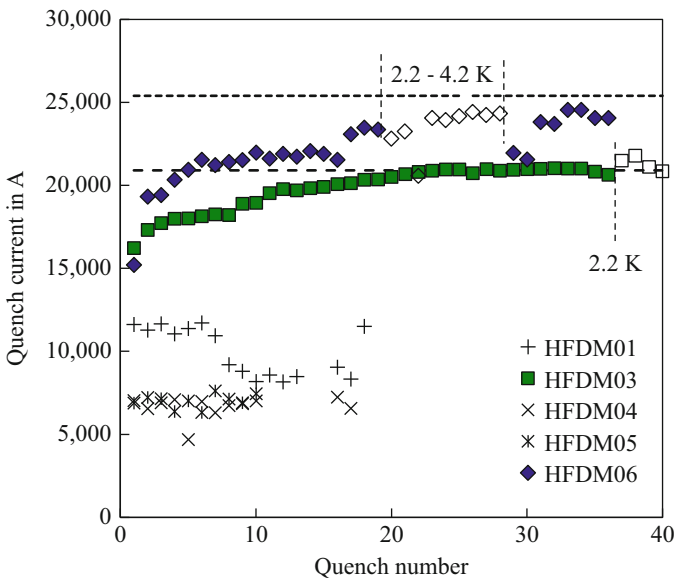


Fig. 7.22 Dipole mirror training at 4.5 K (solid markers) and lower temperatures (open markers). (Zlobin 2011)

7.7.2 *Technology Scale-Up*

Nb₃Sn technology scale-up is a key phase for magnet implementation in accelerators. It addresses problems related to winding, curing, reaction, impregnation, and handling of long Nb₃Sn coils, as well as long magnet assembly and performance. The scale-up was done in two steps, starting in 2006–2007 with fabricating and testing of a 2 m long Nb₃Sn dipole coil made of PIT wire (Zlobin et al. 2007). Then, a year later, the first 4 m long dipole coil made of RRP108/127 Nb₃Sn wire was fabricated and tested (Chlachidze et al. 2009). Pictures of the 4 m long Nb₃Sn coil and dipole mirror are shown in Fig. 7.23.

Training quenches of the 2 m long PIT coil (LM01) and the 4 m long RRP coil (LM02) at 4.5 K are shown in Fig. 7.24, where they are compared with the corresponding 1 m long coils that were also tested in dipole mirror magnets.

The 2 m PIT coil reached its SSL and a field level of 10 T at 4.5 after a short training, similar to the corresponding 1 m long PIT coil tested in dipole mirror HFD03. The 4 m long RRP coil, unlike its short version, was limited at 4.5 K by strong flux jump instabilities in the coil outer layer (perhaps caused by conductor damage during coil fabrication or magnet assembly). After suppressing these instabilities by heating the coil outer layer using quench heaters, however, it reached ~90% of its SSL at 4.5 K. The maximum quench current was limited by quenches in the coil inner-layer mid-plane turns, which were impacted by the heat flux from the heaters.

7.8 Conclusion

Nb₃Sn accelerator dipole magnets based on shell-type coils and the W&R method were developed at FNAL. The twin-aperture magnet designs with horizontal and vertical aperture arrangements and cold and warm iron yokes met the VLHC technical requirements and offered substantial cost reductions for the collider magnet system.

The R&D program experimentally demonstrated the main magnet parameters (maximum field, quench performance, field quality) and their reproducibility using a series of 1 m long single-aperture models, as well as demonstrated the technology scale-up using longer coils. As part of the technology development, nineteen 1 m long two-layer dipole coils were fabricated and tested in six dipole and six dipole mirror models. The last three dipoles and two mirrors reached their design fields of 10–11 T. All six short dipole models showed good, well-understood, and



Fig. 7.23 (a) First in the world 4 m long Nb_3Sn dipole coil. (b) Dipole mirror LM02 with 4 m coil prepared for transportation to the FNAL magnet test facility. (Zlobin 2011)

reproducible field quality. The quench performance and field quality data confirmed the good reproducibility and robustness of the magnet design and technology. It was the first time that Nb_3Sn technology scale-up was performed by building and testing

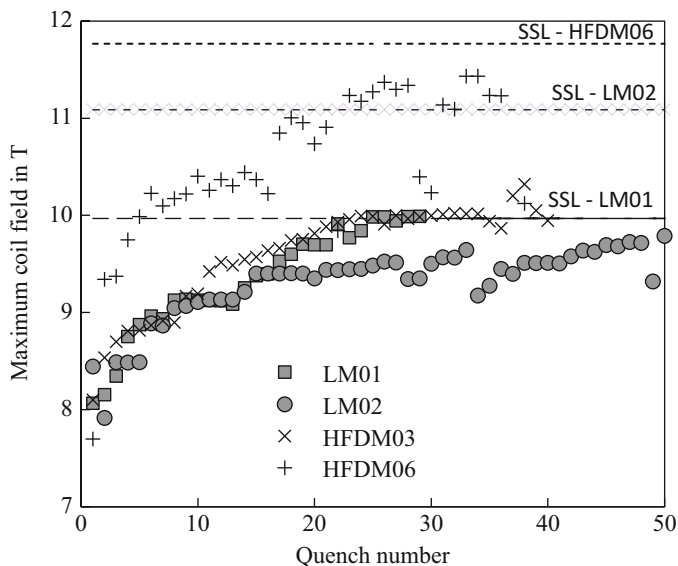


Fig. 7.24 Mirror models training summary at 4.5 K. (Chichili et al. 2004)

2 m and 4 m long dipole coils. The first positive results of the Nb₃Sn technology scale-up phase reinforced high expectations for the practical use of this technology in particle accelerators.

References

- Ambrosio G, Kashikhin VV, Limon PJ et al (2000a) Conceptual design study of high field magnets for very large hadron collider. *IEEE Trans Appl Supercond* 10(1):310–313. <https://doi.org/10.1109/77.828236>
- Ambrosio G, Andreev N, Caspi S et al (2000b) Magnetic design of the Fermilab 11 T Nb₃Sn short dipole model. *IEEE Trans Appl Supercond* 10(1):322–325. <https://doi.org/10.1109/77.828239>
- Ambrosio G, Andreev N, Chichili DR et al (2000c) Mechanical design and analysis of the Fermilab 11 T Nb₃Sn dipole model. *IEEE Trans Appl Supercond* 10(1):306–309. <https://doi.org/10.1109/77.828235>
- Ambrosio G, Andreev N, Arkan TT et al (2000d) Development of the 11 T Nb₃Sn dipole model at Fermilab. *IEEE Trans Appl Supercond* 10(1):298–301. <https://doi.org/10.1109/77.828233>
- Andreev N, Arkan TT, Chichili DR et al (2000) Fabrication and testing of a high field dipole mechanical model. *IEEE Trans Appl Supercond* 10(1):314–317. <https://doi.org/10.1109/77.828237>
- Bossert R, Ambrosio G, Andreev N et al (2010) Development and test of collaring methods for Nb₃Sn quadrupole magnets. In: Weisend JG II, Barclay J, Breon S et al (eds) AIP conference proceedings, 28 June–2 July 2018, Tuscon, vol 1218. American Institute of Physics, Melville, New York, pp 507–514

- Chichili D, Arkan TT, Ozelis JP et al (2000) Investigation of cable insulation and thermo-mechanical properties of Nb₃Sn composite. *IEEE Trans Appl Supercond* 10(1):1317–1320. <https://doi.org/10.1109/77.828478>
- Chichili DR, Ambrosio G, Andreev N et al (2001) Fabrication of the shell-type Nb₃Sn dipole magnet at Fermilab. *IEEE Trans Appl Supercond* 11(1):2160–2163. <https://doi.org/10.1109/77.920285>
- Chichili DR, Ambrosio G, Andreev N et al (2004) Design, fabrication and testing of Nb₃Sn shell type coils in mirror magnet configuration. In: Waynert J, Barclay J, Breon S et al (eds) *Advances in cryogenic engineering: transactions of the cryogenic engineering conference—CEC*, vol 49. American Institute of Physics, Melville, New York, 710:775–782. <https://doi.org/10.1063/1.1774754>
- Chlachidze G, Ambrosio G, Andreev N et al (2009) Quench performance of a 4-m long Nb₃Sn shell-type dipole coil. *IEEE Trans Appl Supercond* 19(3):1217–1220. <https://doi.org/10.1109/tasc.2009.2018276>
- Den Ouden A, Wessel S, Krooshoop E et al (1997) Application of Nb₃Sn superconductors in high-field accelerator magnets. *IEEE Trans Appl Supercond* 7(2):733–738. <https://doi.org/10.1109/77.614608>
- Fermilab (2001) Design study for a staged Very Large Hadron Collider. Fermilab, Batavia, IL, TM-2149, June 4
- Jackson JD (1986) Conceptual design of the superconducting super collider. SSC-SR-2020, SSC Central Design Group, Berkeley
- Kashikhin VV, Zlobin AV (2001) Magnetic designs of 2-in-1 Nb₃Sn dipole magnets for VLHC. *IEEE Trans Appl Supercond* 11(1):2176–2179. <https://doi.org/10.1109/77.920289>
- Kashikhin VV, Barzi E, Chichili D et al (2003) Passive correction of the persistent current effect in Nb₃Sn accelerator magnets. *IEEE Trans Appl Supercond* 13(2):1270–1273. <https://doi.org/10.1109/tasc.2003.812642>
- McInturff AD, Benjergedes R, Bish P et al (1997) Test results for a high field (13 T) Nb₃Sn dipole. In: Comyn M, Craddock MK, Reiser M et al (eds) *Proceedings of the 1997 particle accelerator conference (PAC1997)*, 12–16 May 1997, Vancouver. IEEE, Piscataway, pp 3212–3214
- Parrell JA, Field MB, Zhang Y et al (2005) Advances in Nb₃Sn strand for fusion and particle accelerator applications. *IEEE Trans Appl Supercond* 15(2):1200–1204. <https://doi.org/10.1109/tasc.2005.849531>
- Rice JA, Fabian PE, Hazelton CS et al (1999) Mechanical and electrical properties of wrappable ceramic insulation. *IEEE Trans Appl Supercond* 9(2):220–223. <https://doi.org/10.1109/77.783276>
- Russenschuck S (1995) A computer program for the design of superconducting accelerator magnets. CERN, Sep 1995. CERN, Geneva
- Sabbi G, Ambrosio G, Andreev N et al (2000) Conceptual design of a common coil dipole for VLHC. *IEEE Trans Appl Supercond* 10(1):330–333. <https://doi.org/10.1109/77.828241>
- Yadav S, Chichili DR, Terechkin I (2001) Coil end parts design and fabrication issues for the high field dipole at Fermilab. *IEEE Trans Appl Supercond* 11(1):2284–2287. <https://doi.org/10.1109/77.920316>
- Zlobin AV (2011) Status of Nb₃Sn accelerator magnet R&D at Fermilab. CERN Yellow Report CERN-2011-003. CERN, Geneva, pp 50–58 [arXiv:1108.1869]
- Zlobin AV, Ambrosio G, Andreev N et al (2005) R&D of Nb₃Sn accelerator magnets at Fermilab. *IEEE Trans Appl Supercond* 15(2):1113–1118. <https://doi.org/10.1109/tasc.2005.849507>

- Zlobin AV, Kashikhin VV, Barzi E (2006) Effect of flux jumps in superconductor on Nb₃Sn accelerator magnet performance. *IEEE Trans Appl Supercond* 16(2):1308–1311. <https://doi.org/10.1109/tasc.2006.870557>
- Zlobin AV, Ambrosio G, Andreev N et al (2007) Nb₃Sn accelerator magnet technology R&D at Fermilab. In: Petit-Jean-Genaz C (ed) *Proceedings of 2007 IEEE particle accelerator conference (PAC)*, 25–29 June 2007. Albuquerque, pp 482–484

Open Access This chapter is licensed under the terms of the Creative Commons Attribution 4.0 International License (<http://creativecommons.org/licenses/by/4.0/>), which permits use, sharing, adaptation, distribution and reproduction in any medium or format, as long as you give appropriate credit to the original author(s) and the source, provide a link to the Creative Commons licence and indicate if changes were made.

The images or other third party material in this chapter are included in the chapter's Creative Commons licence, unless indicated otherwise in a credit line to the material. If material is not included in the chapter's Creative Commons licence and your intended use is not permitted by statutory regulation or exceeds the permitted use, you will need to obtain permission directly from the copyright holder.

